X-611-68-92

PREPRINT

NASA TM X- 63147

RING CURRENT PARTICLE DISTRIBUTIONS DERIVED FROM RING CURRENT MAGNETIC FIELD MEASUREMENTS

R. A. HOFFMAN
L. J. CAHILL, JR.

FEBRUARY 1968

GSFC — GODDARD SPACE FLIGHT CENTER —
GREENBELT, MARYLAND

X-611-68-92

PREPRINT

RING CURRENT PARTICLE DISTRIBUTIONS DERIVED FROM RING CURRENT MAGNETIC FIELD MEASUREMENTS

R. A. Hoffman

Goddard Space Flight Center

and

L. J. Cahill, Jr.

University of New Hampshire

February 1968

GODDARD SPACE FLIGHT CENTER

Greenbelt, Maryland

RING CURRENT PARTICLE DISTRIBUTIONS DERIVED FROM RING CURRENT MAGNETIC FIELD MEASUREMENTS

R. A. Hoffman

Goddard Space Flight Center

and

L. J. Cahill, Jr.

University of New Hampshire

February 1968

GODDARD SPACE FLIGHT CENTER

Greenbelt, Maryland

ABSTRACT

The particle energy density distribution for the symmetric portion of the April 17, 1965, magnetic storm has been deduced from the measured ring current magnetic field profile. This distribution contains a basic spatial distribution and a time decay term which is a function of distance in order to accomplish the fit between the calculated magnetic effects of the particles and the measured ring current field over a period of a day. With various assumptions as to the particle loss, the time decay yields the average energy of the particles as a function of distance, and thence the total integral omnidirectional proton flux.

RING CURRENT PARTICLE DISTRIBUTIONS DERIVED FROM RING CURRENT MAGNETIC FIELD MEASUREMENTS

INTRODUCTION

In spite of the fact that satellites have been carrying fields and particles experiments throughout the magnetosphere for almost a decade, it has been only recently that the satellite experiments flown have had the proper orbits and sensitivities to observe the ring current magnetic field and the ring current particles. The Explorer 26 magnetometer first conclusively displayed the location of the ring current and the morphology of its growth and decay, especially for the magnetic storm commencing on April 17, 1965 (Cahill, 1966). Much more recently, utilizing the OGO-3 satellite, Frank (1967) first made measurements of the charged particles actually comprising the ring current, and this constitutes the only measurement to date. Thus many properties of the ring current particles remain unknown, especially the differences in the properties between various storms.

It is desirable, then, to utilize every means available to gain insights into the particle distributions responsible for the main phases. Besides the direct particle measurements, the only other available observations which can yield any details about the ring current particle distributions are the measurements of their magnetic effects.

Unfortunately, while it is relatively straight-forward to calculate the magnetic field resulting from a given distribution of charged particles in the

magnetosphere (Hoffman and Bracken, 1965), the converse is not possible, because the field at a given point in space is an integral depending upon the entire particle distribution. Thus the only scheme available to determine the particle distribution is one of trial and error: begin with a particle energy density distribution model, calculate its magnetic effect, compare the calculated field with the measured field, use the differences as a guide in modifying the model, and repeat the process until a satisfactory fit is achieved.

We used this method to obtain the particle energy density distribution as a function of time for passes during the symmetric phase of the April 17, 1965, magnetic storm. From the particle time decay constant as a function of distance, assuming the loss of particles was due solely to coulomb scattering and charge exchange, we then obtained the average energy of the particles as a function of distance, and thence the integral omnidirectional flux distribution of protons.

SATELLITE DATA

For the purpose of discussing the ring current particle distribution, the main phase of the magnetic storm can be separated into two phases: the asymmetric portion, during which time the main phase develops and a rapid partial recovery takes place, and the ring current particles are asymmetrically distributed in local time; and the symmetric portion, during which time the slower total recovery progresses, and the particles are symmetrically distributed around the earth (Cahill, 1966; Meng and Akasofu, 1967). In relation to D_{st} these phases are shown in Figure 1 for the April 17, 1965, storm.

In this study we will consider only the symmetric phase of the storm, the period after 1200 U.T. on April 18. The series of magnetometer records from Explorer 26 has shown that the storm inflation of the magnetosphere during this phase is a function of L, of magnetic latitude, and of storm time. (During the asymmetric phase, of course, the inflation is strongly dependent also on local time.) On a single pass, then, the ring current field depends upon only two parameters, L and magnetic latitude. Due to the symmetry of the particle motion about the magnetic equator, the latitude effect can be almost eliminated by using data from a very low latitude pass. The ring current magnetic field profile would then be a reflection primarily of the equatorial energy density distribution of the particles, and only secondarily on their pitch angle distributions. The time decay rate of this equatorial distribution can then be obtained by comparing the particle profiles derived from two equatorial passes. Knowing this time decay rate as a function of distance, it would then be possible to investigate in some detail the pitch angle distributions of the particles as a function of distance by utilizing the magnetic field profiles of an equatorial pass and a high latitude pass. It is the first two steps of this process, the equatorial energy density distribution and its decay rate, that will be discussed herein.

The first low latitude pass during the symmetric phase was 376 outbound, early on April 19, and the second such pass was 379 outbound on early April 20 (see Figure 1). Their trajectories in distance and magnetic latitude are shown in Figure 2. We will obtain the particle energy density distributions for these

passes whose magnetic fields are comparable to those measured by the satellite magnetometer.

Unfortunately, the magnetometer cannot select only the ring current magnetic field to measure, but its output is due to the vector sum of magnetic fields from all sources, and these are many. They include, besides the ring current field, the main field from sources internal to the earth, the boundary field, the neutral sheet field, and the earth's induction field from all the external sources. This latter field we neglect as small. Thus

$$\vec{B} = \vec{B}_{main} + \vec{B}_{boundary} + \vec{B}_{neutral\ sheet} + \vec{B}_{ring\ current} \qquad (1)$$

In order to derive the ring current field we must choose models for the other fields and subtract them from the total field measured. For the main field we have used the field model of Cain et al. (1965) (coefficients from Hendricks and Cain, 1966). The boundary and neutral sheet effects are taken from the description by Mead (1964) and Williams and Mead (1965), with the current sheet parameters as follows: front edge, 8 R_E; rear edge, 200 R_E; field strength adjacent to sheet, 16 γ. According to Williams (1967) the boundary during the passes we have chosen had returned to the pre-storm location, and is taken as 10 R_E at the subsolar point.

The calculations were performed on a constant magnetic meridian plane at 186°E magnetic longitude for pass 376 and 202°E longitude for pass 379, which are the average longitudes for the passes. Fortunately in this region of the earth

there is a small longitudinal gradient in the field. The local time for both meridian planes was considered to be 1200 hours, again about the averages for the passes.

The scalar values of the ring current fields for the two passes are plotted in Figure 3 as a function of distance in earth radii. This scalar field is taken as the difference between the absolute value of the measured total field and the absolute value of the vector sum of the main, boundary and neutral sheet fields:

$$B_{\text{measured ring current}} = \left|\vec{B}_{\text{measured}}\right| - \left|\vec{B}_{\text{main}} + \vec{B}_{\text{boundary}} + \vec{B}_{\text{neutral sheet}}\right| \quad (2)$$

Note that a comparison of the data from pass 376 of this figure and Figure 15 of Cahill (1966), which is the measured field minus only the main field, shows that the inclusion of the boundary and neutral sheet fields produces an increase in what is considered the ring current field of about 14γ at three earth radii and 21γ at five earth radii.

Since the measured magnetic profiles obtained with the Explorer 26 magnetometer provide the experimental basis for this report, a brief consideration of the method of obtaining these profiles and the possible inaccuracies in them is in order. Each of the data points $\left|\vec{B}_{\text{measured}}\right|$ reported previously by Cahill (1966) and reproduced here after corrections as Figure 3 was calculated as $\sqrt{B_{\text{axial}}^2 + B_{\text{transverse}}^2}$. $B_{\text{transverse}}$ was the amplitude of a least-squares, sine wave fit to 40 individual (10 millisecond) samples (3 samples per second) from a fluxgate sensor mounted perpendicular to the spin axis. B_{axial} was the average of

a sine wave fitted to 40 samples from a fluxgate sensor approximately aligned with the satellite spin axis. Standard deviations of the axial samples and the transverse samples from the fitted sine waves were typically 2 to 4γ. Possible drift of the transverse magnetometer output for zero magnetic field is not a problem since only the sine wave amplitude is used. Such drift, from pre-flight calibration, was noted to be as great as 10γ. Equivalent drift in the axial sensor might be expected but no correction was made. Because of the relative magnitudes of B_{axial} and $B_{transverse}$ an uncorrected 10γ error in B_{axial} would produce a 5γ error in $|\vec{B}_{measured}|$. In calculating the vector field components other errors such as the uncertainty in spin axis orientation must be considered but do not apply to the record of $|\vec{B}_{measured}|$.

The absolute error of the values of $|\vec{B}_{measured}|$ due to experimental uncertainties is now estimated to be less than ±10γ. In Figure 3 $|\vec{B}_{main} + \vec{B}_{boundary} + \vec{B}_{neutral\ sheet}|$ have been subtracted from $|\vec{B}_{measured}|$; each of these vectors may contribute to error in the corrected magnetic field profiles. The error in $\vec{B}_{main}$ may be estimated as less than ±5γ by consideration of the discrepancies, above 3 R_E, between the fields computed with various sets of harmonic coefficients (Cain et al., 1965). The error in $\vec{B}_{neutral\ sheet}$ is certainly less than the neutral sheet contribution at 3 R_E, about 13γ for the model used here. The boundary is not measured by this satellite experiment and although the 10 R_E chosen is a reasonable location, the boundary is known to vary from 9 R_E to 13 R_E. The location has been observed to expand beyond 13 R_E in the early recovery phase

of a storm and to return to 10 R_E as the storm decays (Cahill and Patel, 1967). A boundary correction of about 10γ must be made for every earth radius the boundary location is in error. Therefore, the total error in $|\vec{B}_{main} + \vec{B}_{boundary} + \vec{B}_{neutral\ sheet}|$ conceivably might be as great as 20γ, raising or lowering the profiles of Figure 3 by that amount.

There is also the possibility that some of the features of the profiles are due to time variations in the magnetosphere field and are not spatial structures to be matched by adjusting the particle energy density. For example, the sharp minimum of the pass 376 profile might be due to a sudden decrease and recovery of field strength, perhaps due to an outbound motion of the boundary. Although some of the bumps on the profiles are certainly due to time variations, the sharp minima and steep slopes of the profiles are seen on both equatorial passes, 376 and 379, and are unlikely to be time variations.

PROCEDURE

The calculation of the magnetic effects of a distribution of charged particles in the magnetosphere in the region of the particles does not have a closed mathematical solution. The ring current field is calculated from the distribution of electric currents, which is derived from the motions of particles in the total magnetic field ($\vec{B}$ of equation 1). But the total magnetic field is not known until the ring current field has been calculated. To obtain a solution to the problem we use the method of successive approximations to the total field: the current distribution for the nth time is calculated for the particles moving in a field

configuration from the previous cycle, the (n - 1)st. When

$$\vec{B}_{\text{ring current}}(n) = \vec{B}_{\text{ring current}}(n-1)$$

a self consistent solution has been obtained. The importance of carrying the calculations beyond the first order has been demonstrated by Hoffman and Bracken (1967), and it is their procedure in carrying out the successive approximations which is used here.

The particle energy density distribution is defined along the magnetic equator in terms of distance and equatorial pitch angle. The normal energy density, ξ_n, due to the normal component of the velocity vector, is given as a series of equations, which remain fixed through all orders of calculations, but are modified to produce a new model whose magnetic field hopefully better fits the measured ring current field. The series of equations always yields a continuous curve, whose derivative is also continuous.

The pitch angle distribution is given by the form $(\sin\alpha)^{2.5}$ where α is the local pitch angle, and the power is independent of distance.

A vector ring current field is calculated from the particle energy density distribution. The equivalent scalar field which may be compared to $B_{\text{measured ring current}}$ of equation 2 is obtained from the following equation:

$$B_{\text{calculated ring current}} = \left|\vec{B}_{\text{main}} + \vec{B}_{\text{boundary}} + \vec{B}_{\text{neutral sheet}} + \vec{B}_{\text{calculated ring current}}\right| - \left|\vec{B}_{\text{main}} + \vec{B}_{\text{boundary}} + \vec{B}_{\text{neutral sheet}}\right| \quad (3)$$

RESULTS

Because of the uncertainties in the determination of the measured ring current field (equation 2), it is more important to obtain a calculated field with similar characteristics than to strive for a minimum absolute difference. The measured fields for passes 376 and 379 have three characteristics which were found to strongly influence the particle profile:

(1) the maximum in each profile is rather sharp,

(2) the outside slopes are quite straight,

(3) except near the maximum on the inside, where the recovery is rather rapid, the inside slopes are also quite straight.

To achieve similar characteristics in the calculated field for pass 376, about 20 different models were tested. The final particle energy density profile accepted is described by three equations in the logarithm of the energy density normal to the magnetic field, ξ_p:

$$\left.\begin{aligned}
&\text{for } 2.29 \leq R < 3.5 \\
&\log \xi_p = 1.54083\,R^3 - 14.77081\,R^2 + 47.48159\,R - 57.16249 \\
&\text{for } 3.5 \leq R < 3.85 \\
&\log \xi_p = 1.94027\,R^3 - 22.67625\,R^2 + 88.14037\,R - 119.75242 \\
&\text{for } 3.85 \leq R \leq 8.0 \\
&\log \xi_p = -2.06786 \times 10^{-2}\,R^2 - 2.87962 \times 10^{-2}\,R - 5.38894
\end{aligned}\right\} \quad (4)$$

The total profile is given in Figure 4, along with the ratios of the particle energy density to the energy density of the dipole field, and to the energy density of the total magnetic field, including the fourth order ring current field. Note that this latter ratio, usually known as β, reaches a value of two in the region of 5 to 6 earth radii; i.e., the particle energy density is twice the total field energy density. The ability of the geomagnetic field to contain particles whose energy density is larger than the magnetic field energy density over a region of the magnetosphere was previously demonstrated (Hoffman and Bracken, 1967).

A discussion of the electric currents produced by this particle distribution is given in the last section.

A comparison of the ring current field calculated to the fourth order from the particle distribution and the measured field during pass 376 is shown in Figure 5. Also shown is the first order calculated field, which is considerably larger in magnitude along the entire orbit than the fourth order, and illustrates the necessity of carrying such calculations to the higher orders. There was negligible difference between the third and fourth orders.

The average difference between the calculated highest order and the measured field was only 3.4γ and the average percentage difference was about 5%. The major discrepancies between the two curves remained in the region inside the maximum ring current field and near apogee.

It was to this particle profile that a time decay was added of the form $\exp\left(-T/T_0\right)$ in order to obtain a new particle profile which produced a magnetic

field similar to the field measured on pass 379. The quantity T equaled 22.8 hours, the time interval between passes 376 and 379, and T_0, a function of distance, was adjusted by trial and error to give the necessary particle distribution. The final function T_0 is given in Figure 6. Inside four earth radii the decay rate for the particles rapidly decreased, reflecting the fact that the magnetic field on the inner side of the maximum ring current field decreased by a larger percentage than on the outside of the maximum.

The agreement between the calculated field from the decayed particle distribution and the measured field for pass 379 is even better than the fit for pass 376 (Figure 7), showing an average difference of only 2.7γ along the orbit.

If the assumption is made that the particle decay is due to charge exchange and coulomb scattering, the average energy of the particles as a function of distance can be obtained from the value of T_0 and the lifetimes calculated by Liemohn (1961). This average energy is also plotted in Figure 6. Out to five earth radii charge exchange is the limiting process on the lifetime of the particles. Of course there is the additional assumption that no new particles or energy were injected into the ring current region in the interval between the two passes. The possibility of such an injection can be determined by investigating the AE index of Davis and Sugiura (1966). Davis and Parthasarathy (1967) proposed that a necessary, though not a sufficient condition for injection, is a large value of this index, which is a measure of auroral activity, although the converse is not necessarily true: that a large AE index definitely means injection. During the

period between the two passes under consideration this index did indicate three bursts of activity coincident with the three small negative excursions of D_{st} at about 1000, 1700, and 2200 U.T. on April 19 (D. H. Fairfield, private communication). Therefore, injection of new particles or energy into the ring current region may have occurred between the two passes being considered. Thus the T_0 values should probably be smaller than those calculated, which would yield smaller values of $\bar{E}$, the average energy of the particles.

The very rapid decrease in the average energy of the particles beyond four earth radii may indicate that processes other than charge exchange or coulomb scattering are shortening the lifetimes of the particles. If other mechanisms are operating the true average energies in this region would be larger than those calculated. Therefore, out to about four earth radii, the $\bar{E}$ in Figure 6 is probably an upper limit, while beyond this distance, it may not decrease in value as rapidly as shown.

From the energy density distribution and assuming the validity of the average energies, we can obtain a rough idea of the total integral omnidirectional flux of protons at the equator as a function of distance. This is plotted in Figure 8 and shows a maximum of about 3×10^9 protons/cm^2-sec at 3.75 earth radii. If one assumes that the average energies of the protons beyond four earth radii are actually larger than those calculated from the lifetimes of the particles, the particle intensities will decrease in the region from four to five earth radii, rather than remain level. An estimate of these fluxes is shown in Figure 8 as

the dashed curve, in which the average energies are based on an extrapolation of the $\bar{E}$ curve in Figure 6 from the data below four earth radii. Since the conversion from energy density to particle flux depends upon $\bar{E}^{-1/2}$, an error in $\bar{E}$ of a factor of two causes an error of only 40% in the flux estimates.

From the particle energy density distributions during passes 376 and 379 the ring current magnetic field was calculated at the surface of the earth. The values of this field are compared with D_{st} on Figure 1 (x's) and show agreement to a few gammas. However, these contributions to D_{st} are augmented by an induction field within the earth. The appropriate correction factor for a field change of one day time constant is 1.4 (Chapman and Price, 1930). This correction moves the calculated values below the observed D_{st} values. One is tempted to extrapolate the particle distribution to the beginning of the symmetric phase of the storm of about 1200 hours on April 18 using the calculated particle lifetimes. This extrapolated value of the ring current magnetic field is also indicated in Figure 1, and shows too low a value for the field, as expected. Besides the necessary correction for the induction field, the average energies of the particles during this earlier period should be considerably lower than those calculated between passes 376 and 379, because the low energy end of the injected particle spectrum should decay more rapidly than the higher energies, leaving a harder spectrum as a function of time.

PARTICLE ENERGY DENSITY PROFILES AND THEIR MAGNETIC FIELDS

It was previously mentioned that about 20 different models of particle energy density distributions were tested before arriving upon the model described for pass 376 in the previous section, which displayed the basic characteristics of the measured ring current field. While each magnetic field profile calculated from a particular model was used as a guide in attempting to improve the succeeding model, considerable trial and error still prevailed because of the one basic difficulty in understanding in a qualitative way the ring current field calculations: the change in the particle distribution in a local region of space may only change the electric currents in that region, but the currents affect the field in the entire ring current region, because the field at a point in space is an integral over the currents in all space.

However, the experience with performing the calculations has exposed certain basic properties of ring current fields in terms of the associated particle distributions. Some of these properties will be described.

1) Initial models.

Influenced by the energy density distribution of the quiet time proton belt for protons with energies greater than 100 kev (Hoffman and Bracken, 1965), and the model ring current work of Hoffman and Bracken (1967), the initial models tested contained the following characteristics: the maximum in the energy density distribution was very rounded, and the decrease in intensity on the outside of the belt was rapid, being a constant ratio to the dipole field energy density ($\propto 1/R^6$), as displayed in Figure 9 (model 1).

The electric current distribution at the equator had a typical broad eastward current maximum, but a rather sharp westward maximum only a few tenths of an earth radius outside the maximum energy density (see Figure 10).

The predominant feature of the magnetic field profile at the equator was the very rapid recovery of the field on the outside of the belt, with a crossover from a negative to positive field in the vicinity of 5¼ earth radii (Figure 11). Aside from this fast outside recovery, the maximum was somewhat broader than those measured on passes 376 and 379.

2) High density tail

The method of keeping the magnetic field from recovering too rapidly on the outside of the belt was suggested by the particle energy density distribution published by Frank (1967) for the July 9, 1966, magnetic storm (see his Figure 7). The primary characteristic of this type of model is the nearly linear decrease in the logarithm of the energy density with distance on the outer side of the belt. A similar model (model 2, Figure 9) with the position of the maximum density moved out a half earth radius from that measured by Frank was tested. It displayed a completely different electric current profile from model 1, as shown also in Figure 10.

A comparison of these two particle distributions and their respective currents clearly displays a most important physical reason for the existence of the currents: an edge effect. This effect depends upon the gradient of the particle distribution and is illustrated schematically for the region on the inner side of the belt in Figure 12.

The first particle profile (model 1) has a rounded maximum, causing on the inner side of the particle distribution (near 3 R_E) a slope which is not large in the region of high particle density. Hence, the eastward current is broad and not as large in magnitude as the westward current. In the region of four earth radii, the slope of the ξ_p profile is maximum on the outer side of the particle distribution. With this also being a high flux region, the westward current is maximum. (These interpretations depend upon the ξ_p profile, whereas Figure 9 contains ξ_p plotted logarithmically.) On the other hand, with the Frank type model (model 2) the particles drop off rapidly on the inner side of the particle distribution from 3.0 to 3.6 R_E near the maximum energy density. Thus, the eastward current maximum is sharp and large in magnitude. The outside slope from 4 to 5 R_E of the energy density distribution is much smaller than for the first model, and the flux remains higher at larger distances, so the westward current extends over a broader region.

The magnetic field profiles correspondingly reflect the different current distribution. The ring current field stays negative to much larger distances for the second model (Figure 11).

3) Sharpness of maximum

The sharpness of the maximum of the ring current field is especially characterized by the rapid recovery of the field on the inner side of the maximum. To achieve this rapid recovery, a very narrow but intense region of eastward current is required in close proximity to the crossover from east to west

currents. This is achieved by using an energy density profile which has an initial rapid decrease in intensity inside the maximum, so that the gradient in particle energy density is large there. Such a particle distribution is shown in Figure 13, (model 3) with its current profile in Figure 14.

For this case tested, the magnitude of the eastward current spike is too large, causing too rapid a recovery in the field in the region of 3 to 3½ earth radii, as shown in Figure 15.

4) Inside recovery

To achieve the nearly linear recovery after the initial rapid recovery inside the maximum of the ring current field, it is necessary to decrease the intensity of the eastward current peak in model 3, but retain its narrow width, and produce a lower level, broader region of eastward current inside the peak. This can be achieved by placing more particles inside about 3¼ earth radii and down to 2.3 earth radii, but keeping the large gradient for the initial fall-off. This produces an inflection in the energy density distribution in the region of 3 earth radii (model 4 in Figure 13), but the model properly gives a lower, broader eastward current in the region from 2¼ to 3¼ earth radii (Figure 14), and therefore the slower, more linear recovery of the field in this region as shown in Figure 15.

The total electric current distribution is pictured in Figure 16. The double lobed eastward current from the inflection in the particle profile near three earth radii clearly stands out. The severe weakening of the current in the region

around the equator from 4 to 5½ earth radii is due to the decrease in the total field strength in which the particles move, and thus a decrease in the diamagnetism of the particles.

SUMMARY

Starting with magnetic profiles obtained from equatorial satellite passes in the recovery phase of a substantial magnetic storm, an energy density profile of the charged particles that produced the magnetic profiles has been calculated by a trial and error method. The energy density profile has interesting features not present in the profiles assumed in earlier studies (for example Akasofu, Cain and Chapman, 1962). The features, in comparison with the earlier models, include a more gradual decrease in energy density on the outside of the peak energy, a steeper initial decrease in energy density inside the peak and a point of inflection on the inner slope.

In the process of matching energy density profiles to magnetic field profiles, procedures of general applicability have been developed. Even though the profiles for this storm may be unique the procedures will be useful for further study with other storm profiles.

Considering the change in the particle energy density profile with time, a time decay constant for the particle energy density was computed. The time constant computed increases with distance to 4 R_E then remains constant. The change in time constant at 4 R_E is particularly interesting because the plasmapause is located near this distance.

If the further assumption is made that charge exchange is the particle decay mechanism, the average particle energy as a function of distance was calculated from the time decay constant. Knowing this average energy, and the energy flux, the integral omnidirectional proton flux was derived.

Since the successful acquisition of appropriate magnetic field data with complete low energy particle data from a satellite during a magnetic storm has not been achieved, the methods applied here should be useful in obtaining particle energy density profiles from the magnetic measurements, and conversely in predicting magnetic profiles from measured particle energy densities.

ACKNOWLEDGMENTS

The assistance of Mr. Fred Berko in performing the computer runs and analyzing their results is acknowledged. The work at the University of New Hampshire was supported by the National Aeronautics and Space Administration under Grant NsG-624.

REFERENCES

Akasofu, S.-I., J. C. Cain and S. Chapman, The magnetic field of the quiet-time proton belt, J. Geophys. Res., 67, 2645-2647, 1962.

Cahill, L. J., Jr., Inflation of the inner magnetosphere during a magnetic storm, J. Geophys. Res., 71, 4505-4519, 1966.

Cahill, L. J., Jr., and V. L. Patel, The boundary of the geomagnetic field, August to November, 1961, Planet. Space Sci., 15, 997-1033, 1967.

Cain, J. C., W. E. Daniels, S. J. Hendricks, and D. C. Jensen, An evaluation of the main geomagnetic field, 1940-1962, J. Geophys. Res., 70, 3647-3674, 1965.

Chapman, S., and A. T. Price, The electric and magnetic state of the interior of the earth, as inferred from terrestrial magnetic variations, Phil. Trans. Roy. Soc. London, A, 229, 427-460, 1930.

Davis, T. N., and R. Parthasarathy, The relationship between polar magnetic activity DP and growth of the geomagnetic ring current, J. Geophys. Res., 72, 5825-5836, 1967.

Davis, T. N., and M. Sugiura, Auroral electrojet activity index AE and its universal time variations, J. Geophys. Res., 71, 785-801, 1966.

Frank, L. A.; On the extraterrestrial ring current during geomagnetic storms, J. Geophys. Res., 72, 3753-3768, 1967.

Hendricks, S. J., and J. C. Cain, Magnetic field data for trapped-particle evaluation, J. Geophys. Res., 71, 346-347, 1966.

Hoffman, R. A., and P. A. Bracken, Magnetic effects of the quiet-time proton belt, J. Geophys. Res., 70, 3541-3556, 1965.

Hoffman, R. A., and P. A. Bracken, Higher order ring currents and particle energy storage in the magnetosphere, J. Geophys. Res., 72, 6039-6050, 1967.

Liemohn, H., The lifetime of radiation belt protons with energies between 1 kev and 1 mev, J. Geophys. Res., 66, 3593-3595, 1961.

Mead, G. D., Deformation of the geomagnetic field by the solar wind, J. Geophys. Res., 69, 1181-1195, 1964.

Meng, C.-I., and S.-I. Akasofu, The geomagnetic storm of April 17-18, 1965, J. Geophys. Res., 72, 4905-4916, 1967.

Williams, D. J., On the low-altitude trapped electron boundary collapse during magnetic storms, J. Geophys. Res., 72, 1644-1646, 1967.

Williams, D. J., and G. D. Mead, Nightside magnetosphere configuration as obtained from trapped electrons at 1100 kilometers, J. Geophys. Res., 70, 3017-3029, 1965.

FIGURE CAPTIONS

Figure 1. D_{st} for the magnetic storm commencing on April 17, 1965, with the asymmetric and symmetric phases of the ring current marked. The times of passes 376 outbound and 379 outbound are also indicated.

Figure 2. The trajectory of passes 376 and 379 in distance in earth radii and magnetic latitude.

Figure 3. Scalar values of the ring current fields for the two passes 376 and 379 obtained from the magnetometer aboard Explorer 26.

Figure 4. The particle energy density distribution at the equator which produces a magnetic field along the trajectory of pass 376 of the Explorer 26 satellite comparable to the ring current magnetic field measured by the magnetometer aboard. Also shown are the ratios of this energy density to the energy density of the dipole field and of the total magnetic field, including the fourth order ring current field.

Figure 5. The first and fourth order magnetic fields along the trajectory of pass 376 calculated from the particle distribution shown in Figure 4, and the measured ring current field. The fields are defined by equations 3 and 2 respectively.

Figure 6. The lifetimes of the particles as a function of distance, T_0, during the time between passes 376 and 379, and the average energy of the particles, $\bar{E}$.

Figure 7. Comparison of the calculated field from the decayed particle distribution and the measured field for pass 379.

Figure 8. The total integral omnidirectional flux of protons at the equator as a function of distance during pass 376, obtained from the energy density distribution and average energies of the particles.

Figure 9. First two types of model particle distributions tested to compare their magnetic fields with that measured during pass 376. Model 1 resembles that of the quiet time proton belt in 1961, and model 2 was based on the energy density distribution measured by Frank (1967) during the storm of July 9, 1966.

Figure 10. Electric current distributions at the equator calculated from the particle models 1 and 2.

Figure 11. Magnetic fields along the orbit of pass 376 calculated from the particle models 1 and 2.

Figure 12. The source of current arising from the gradient of the particle distribution. If the particle intensity about the line of force further away from the earth exceeds that about the closer line, indicated by the relative weights of the gyration circles, a net eastward current results in the region between the two lines of force.

Figure 13. Two other types of model particle distributions tested to compare their magnetic fields with that measured during pass 376. Model 3 contains a very rapid initial decrease in particle intensity inside the maximum, and model 4 is the model accepted as giving the best fit.

Figure 14. Electric current distributions at the equator calculated from the particle models 3 and 4.

Figure 15. Magnetic fields along the orbit of pass 376 calculated from the particle models 3 and 4.

Figure 16. A map of the third order electric current distribution on a magnetic meridian plane for model 4. The currents are in units of 10^{-3} esu/cm^2-sec.

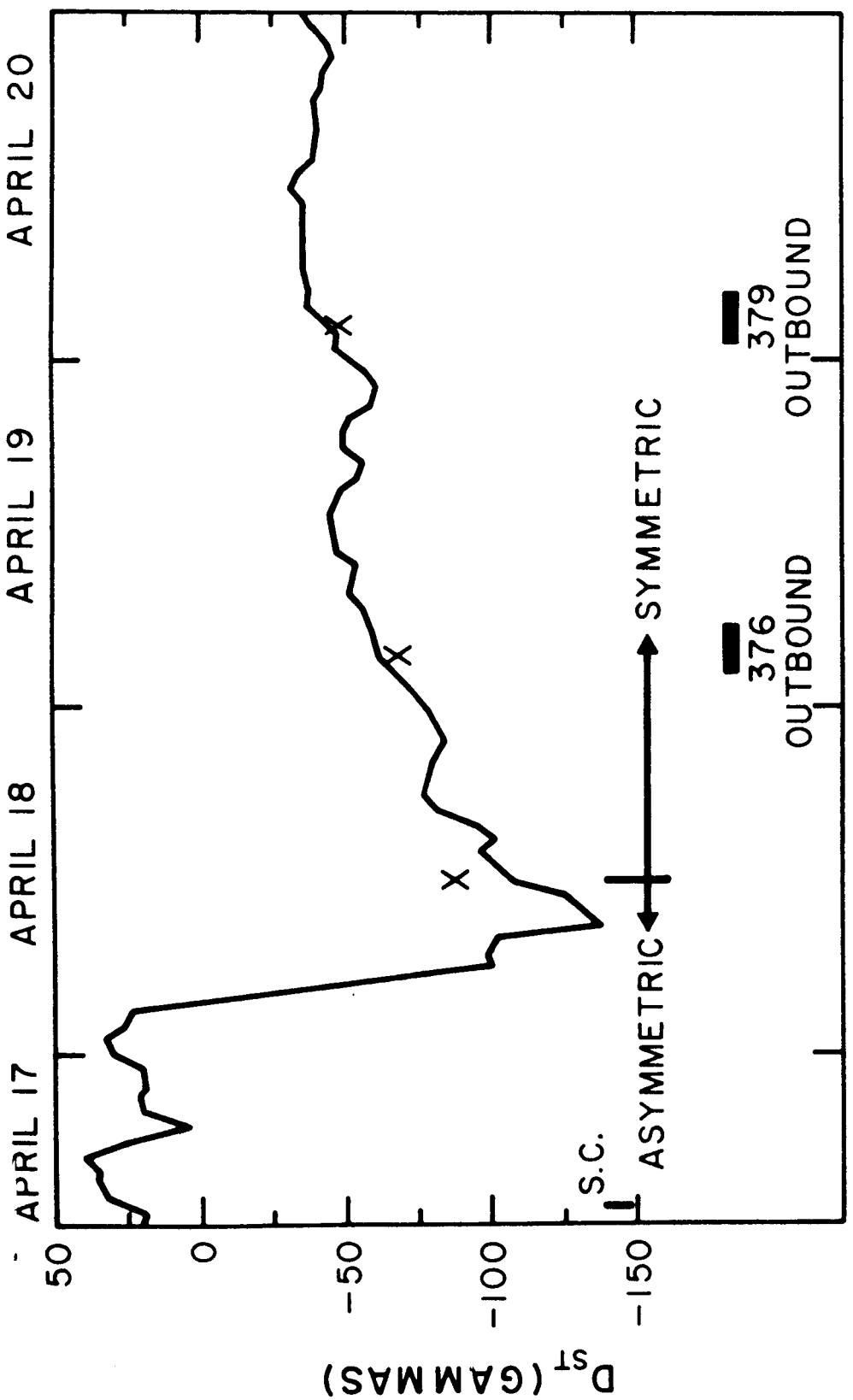
APRIL 17
APRIL 18
APRIL 19
APRIL 20
50
0
-50
-100
-150
D_{ST} (GAMMAS)
S.C.
ASYMMETRIC
SYMMETRIC
376
OUTBOUND
379
OUTBOUND

Figure 1

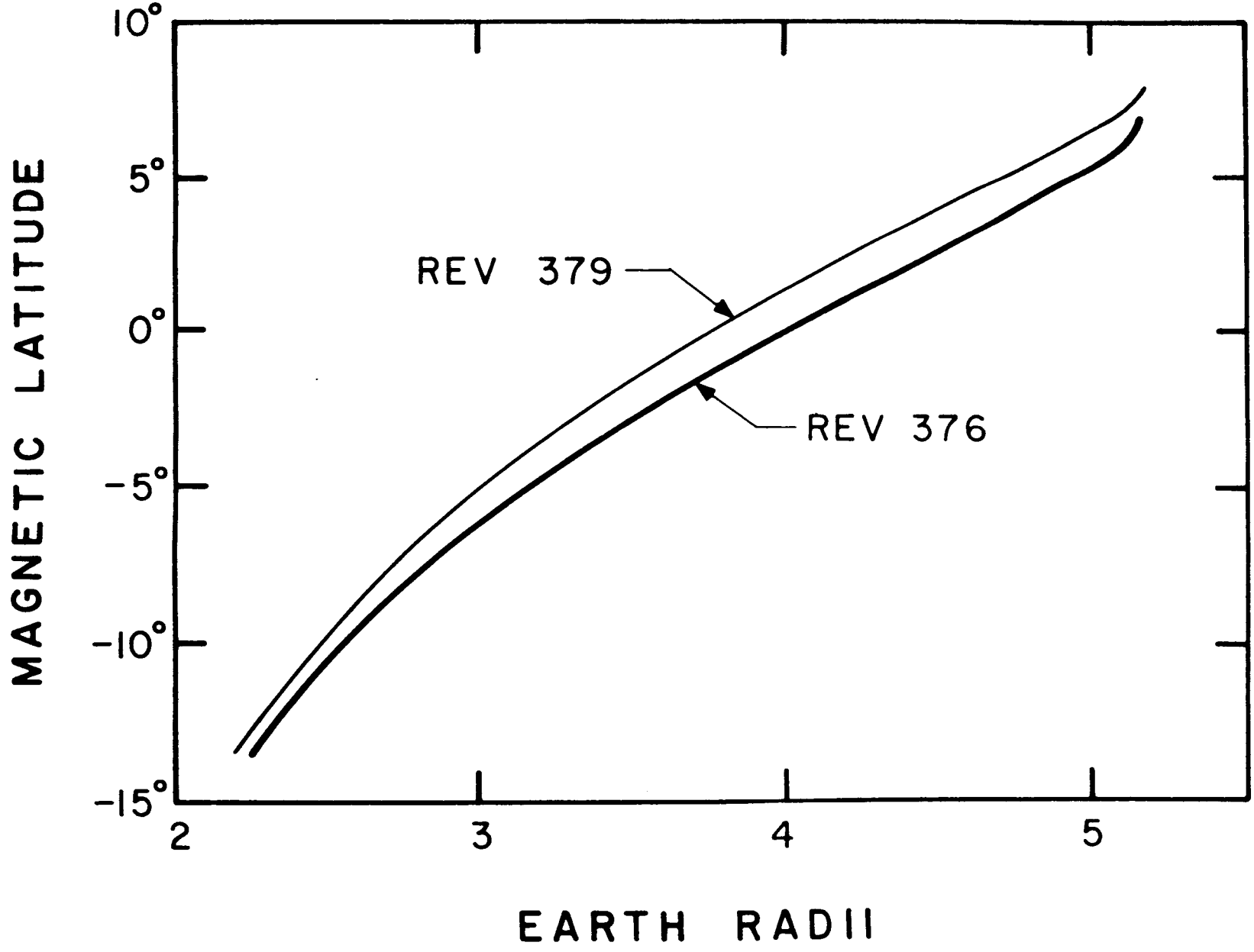
10°
5°
0°
-5°
-10°
-15°
MAGNETIC LATITUDE
REV 379
REV 376
2
3
4
5
EARTH RADII

Figure 2

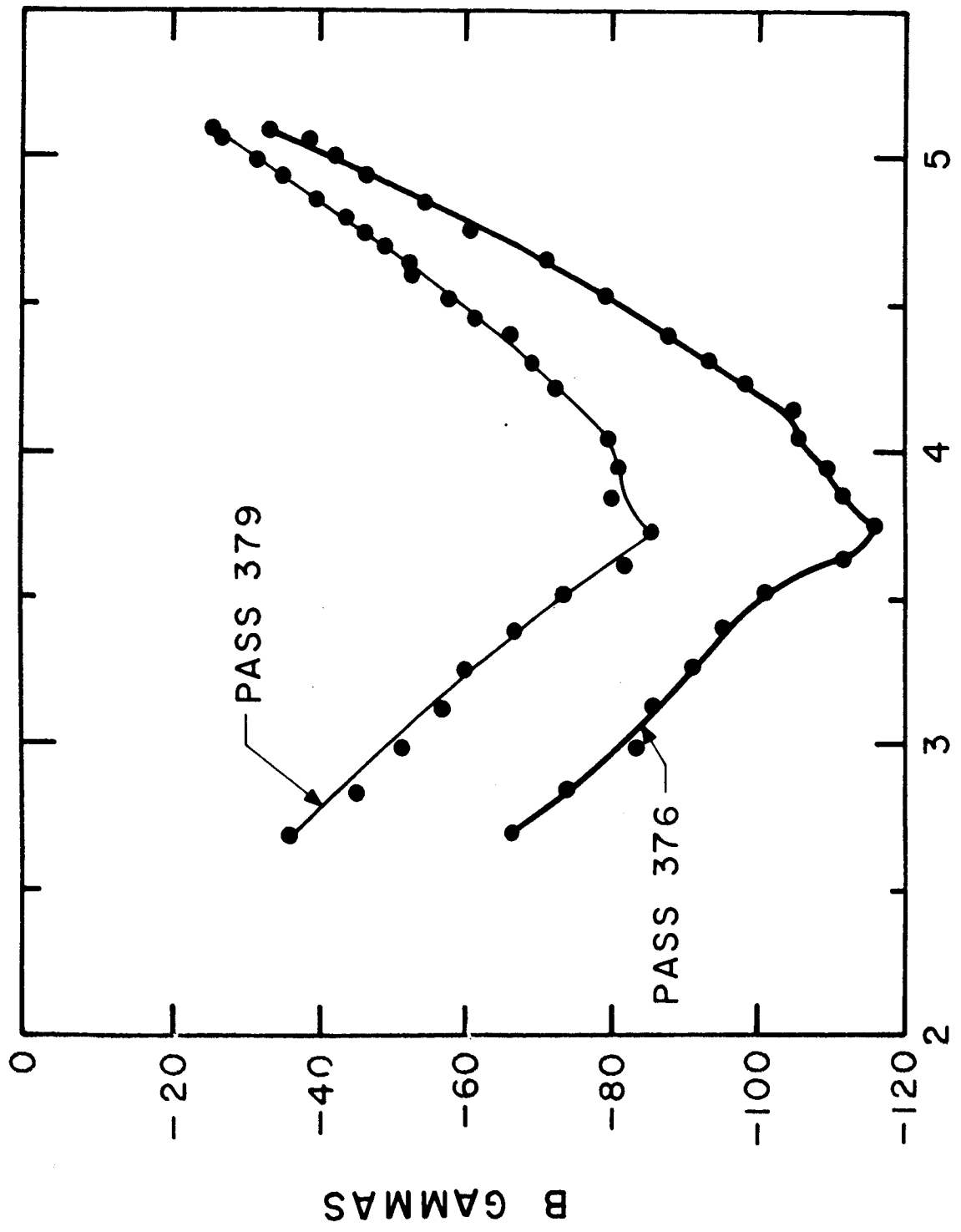
B GAMMAS
0
-20
-40
-60
-80
-100
-120
2
3
4
5
EARTH RADII
PASS 379
PASS 376

Figure 3

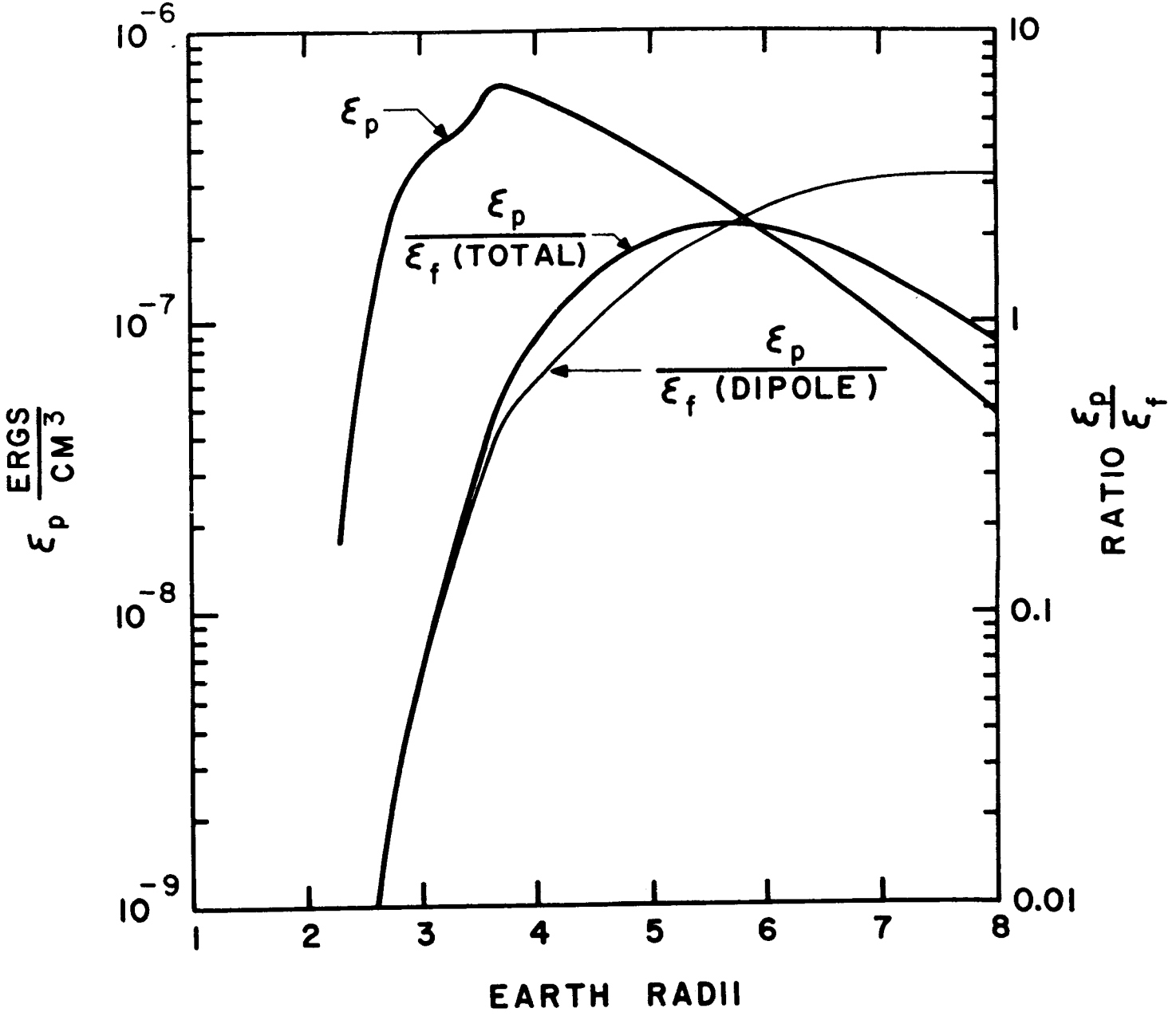
10^{-6}
10^{-7}
10^{-8}
10^{-9}
10
1
0.1
0.01
ε_p
$\frac{\varepsilon_p}{\varepsilon_f\ (TOTAL)}$
$\frac{\varepsilon_p}{\varepsilon_f\ (DIPOLE)}$
$\varepsilon_p \frac{ERGS}{CM^3}$
RATIO $\frac{\varepsilon_p}{\varepsilon_f}$
1
2
3
4
5
6
7
8
EARTH RADII

Figure 4

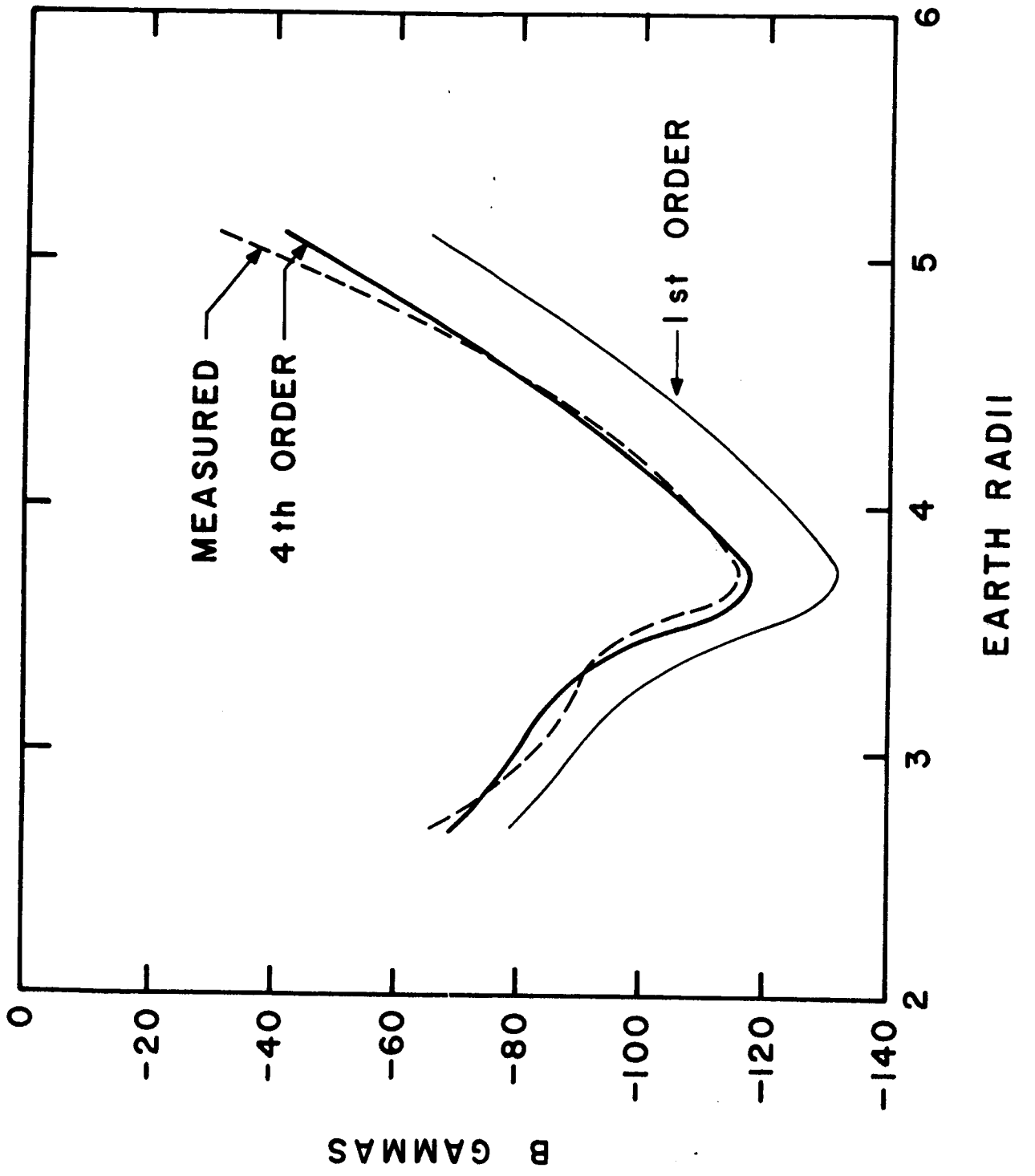
MEASURED
4th ORDER
1st ORDER
B GAMMAS
0
-20
-40
-60
-80
-100
-120
-140
2
3
4
5
6
EARTH RADII

Figure 5

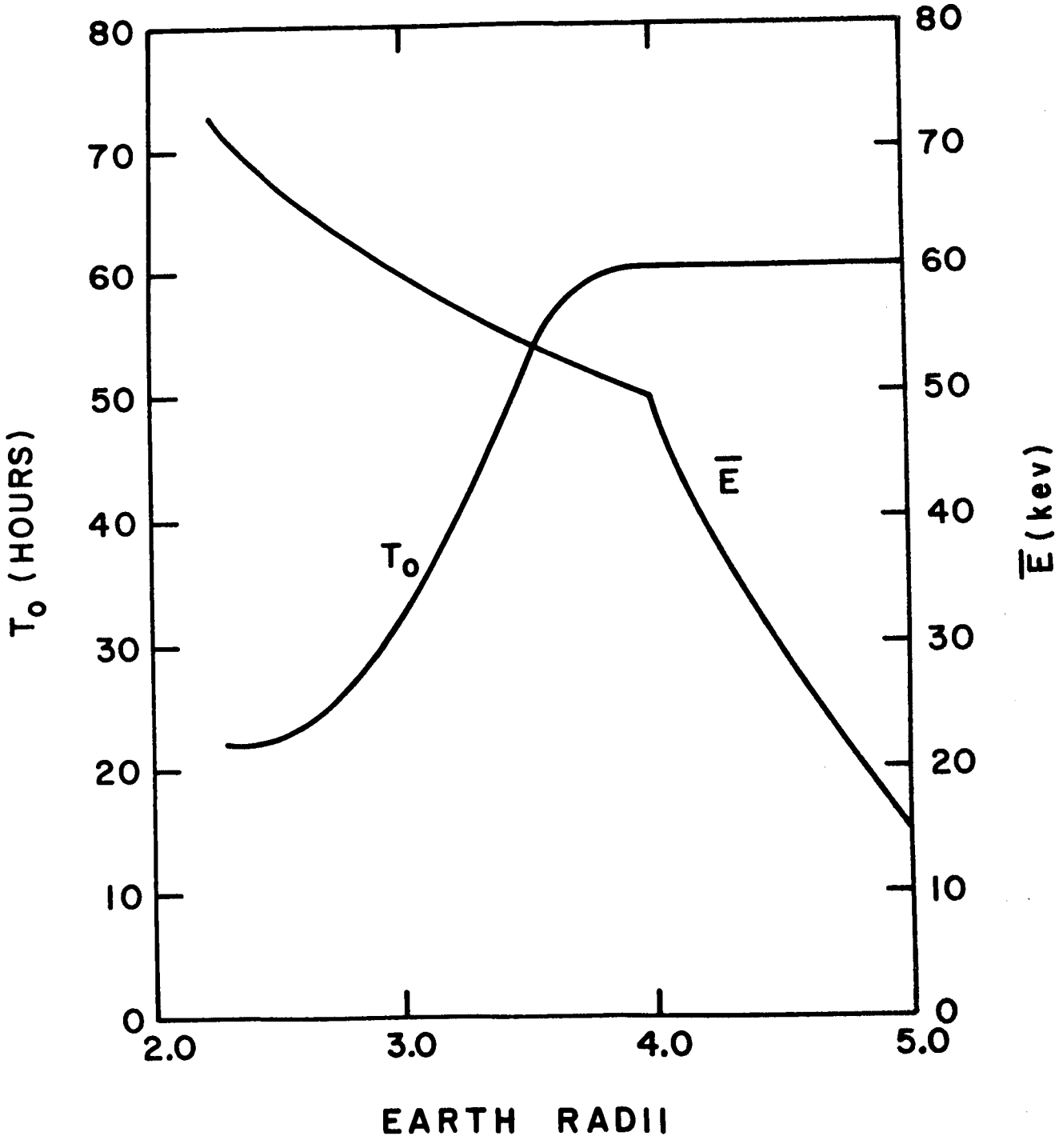
80
70
60
50
40
30
20
10
0
T_0 (HOURS)
T_0
$\bar{E}$
$\bar{E}$ (kev)
2.0
3.0
4.0
5.0
EARTH RADII

Figure 6

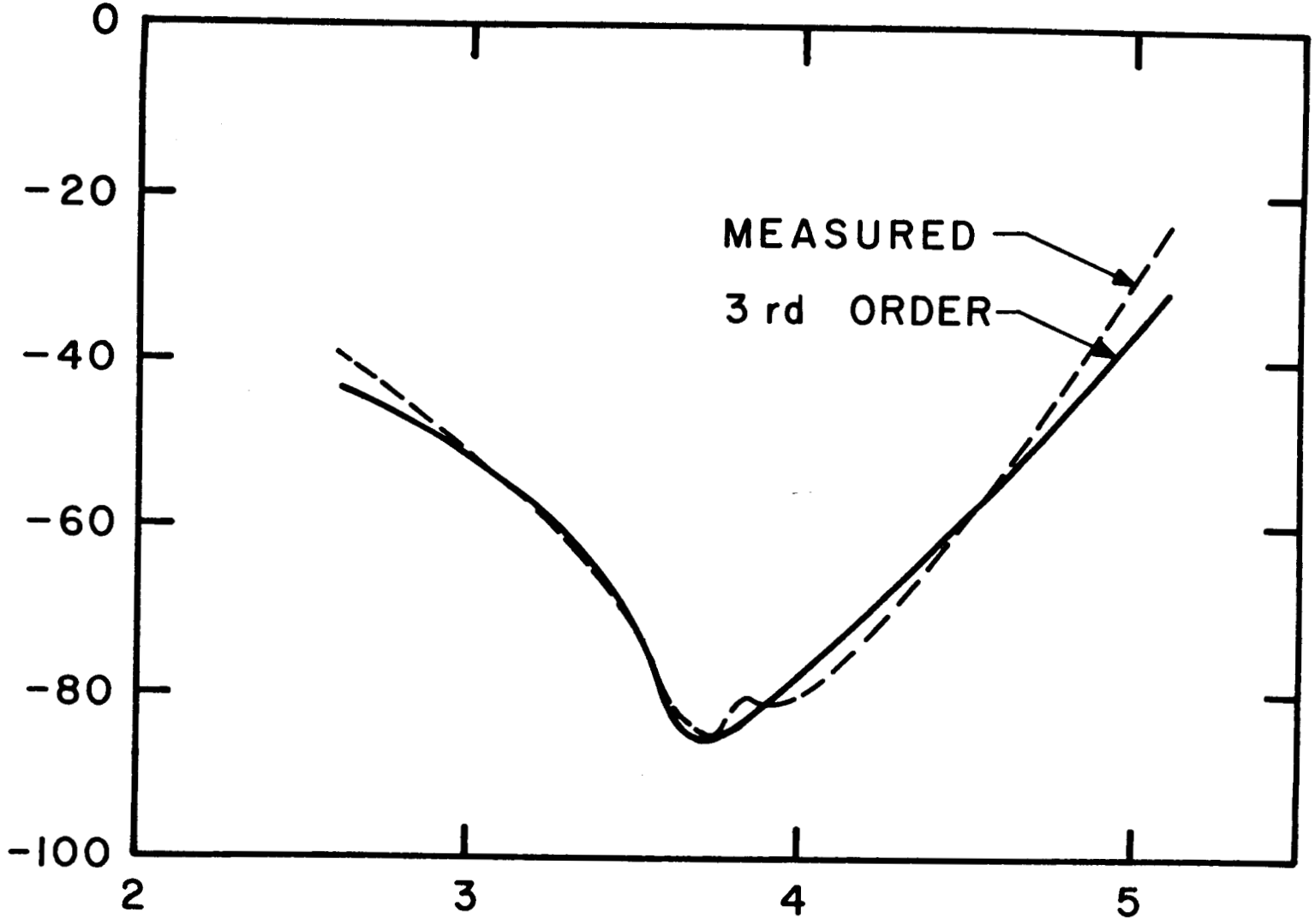

Figure 7

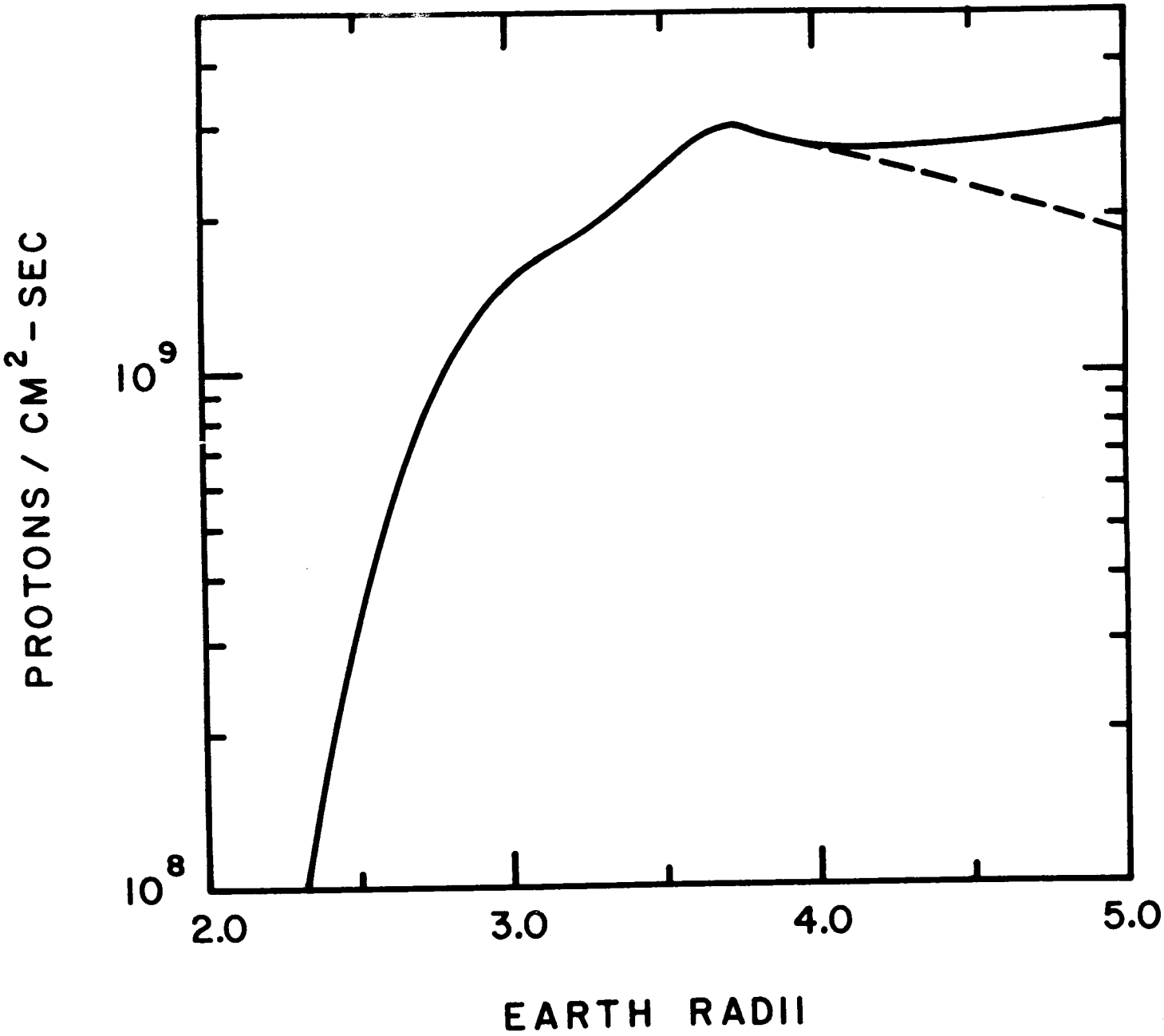

Figure 8

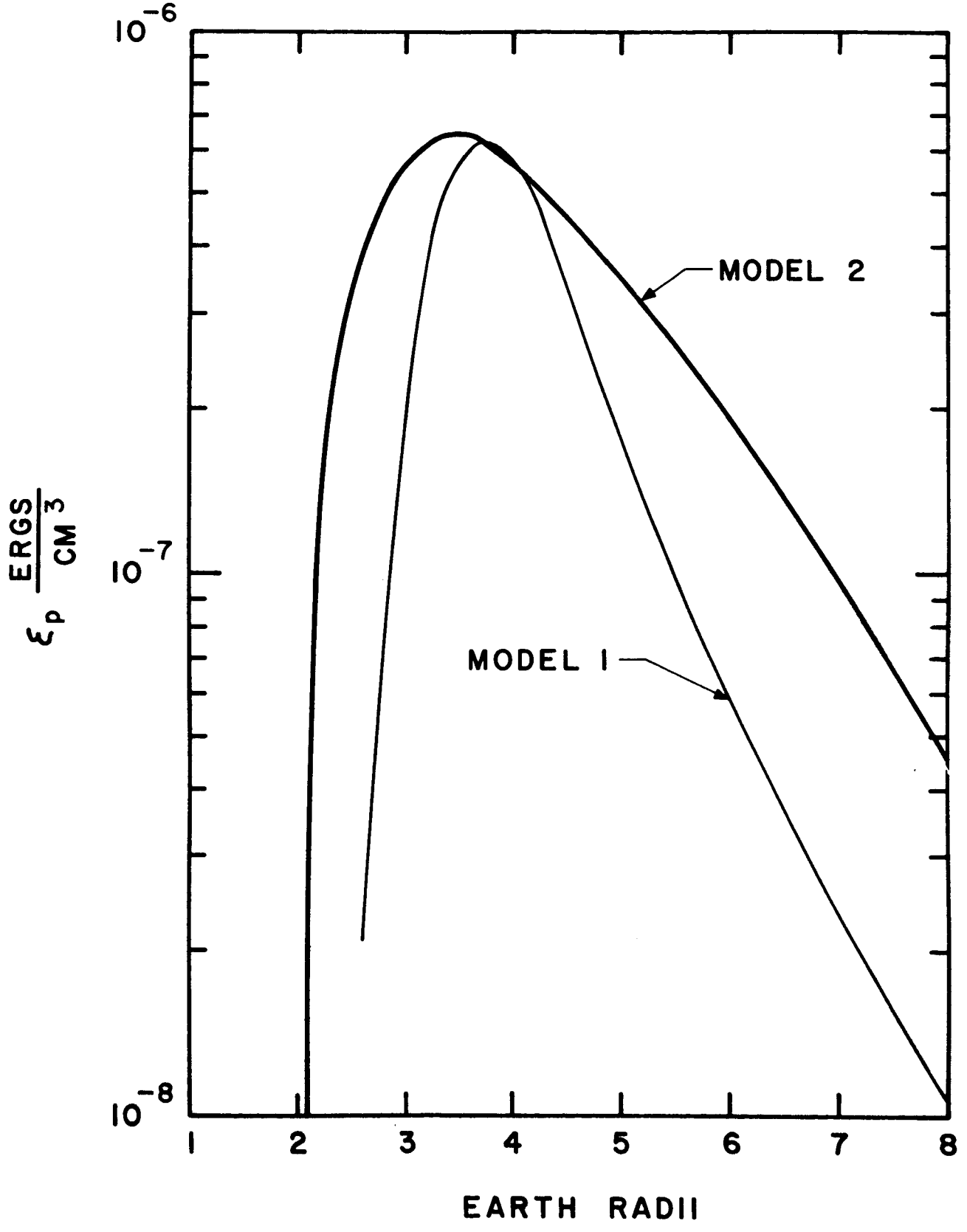
10^{-6}
10^{-7}
10^{-8}
$\xi_p \frac{ERGS}{CM^3}$
MODEL 2
MODEL 1
1
2
3
4
5
6
7
8
EARTH RADII

Figure 9

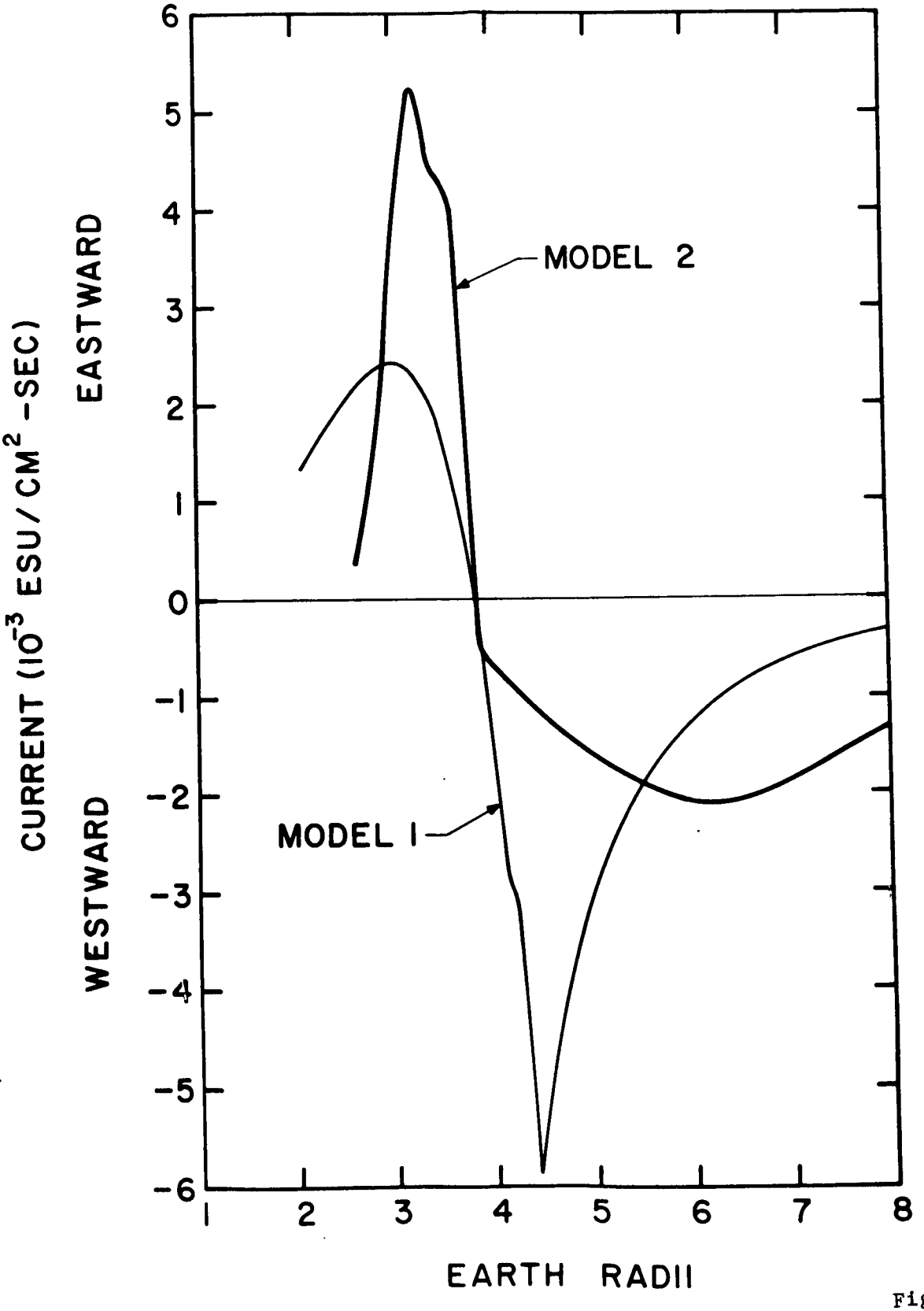
CURRENT (10^{-3} ESU/CM^2-SEC)
EASTWARD
WESTWARD
6
5
4
3
2
1
0
-1
-2
-3
-4
-5
-6
MODEL 2
MODEL 1
1
2
3
4
5
6
7
8
EARTH RADII

Figure 10

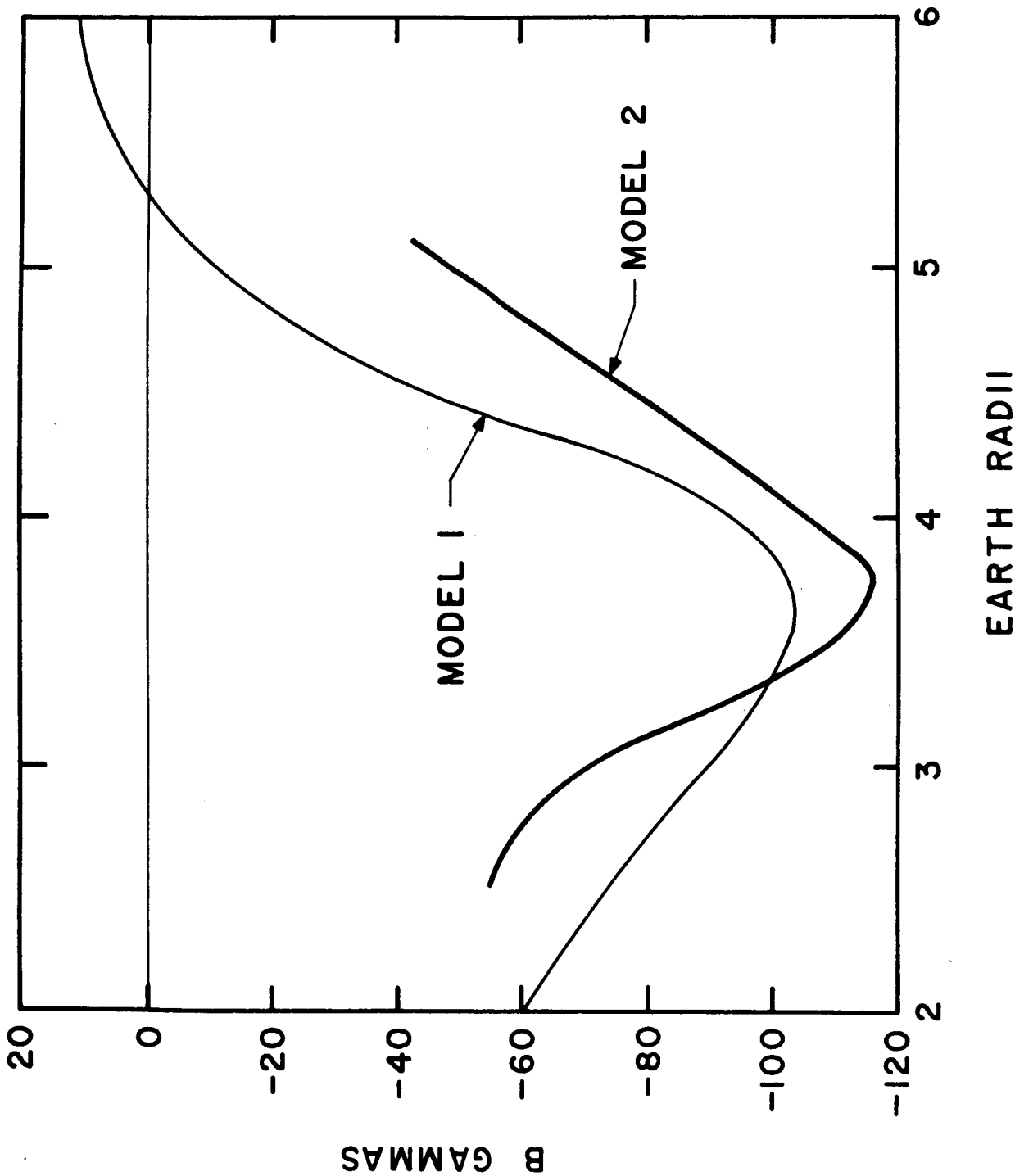
MODEL 2
MODEL 1
B GAMMAS
20
0
-20
-40
-60
-80
-100
-120
2
3
4
5
6
EARTH RADII

Figure 11

Figure 12

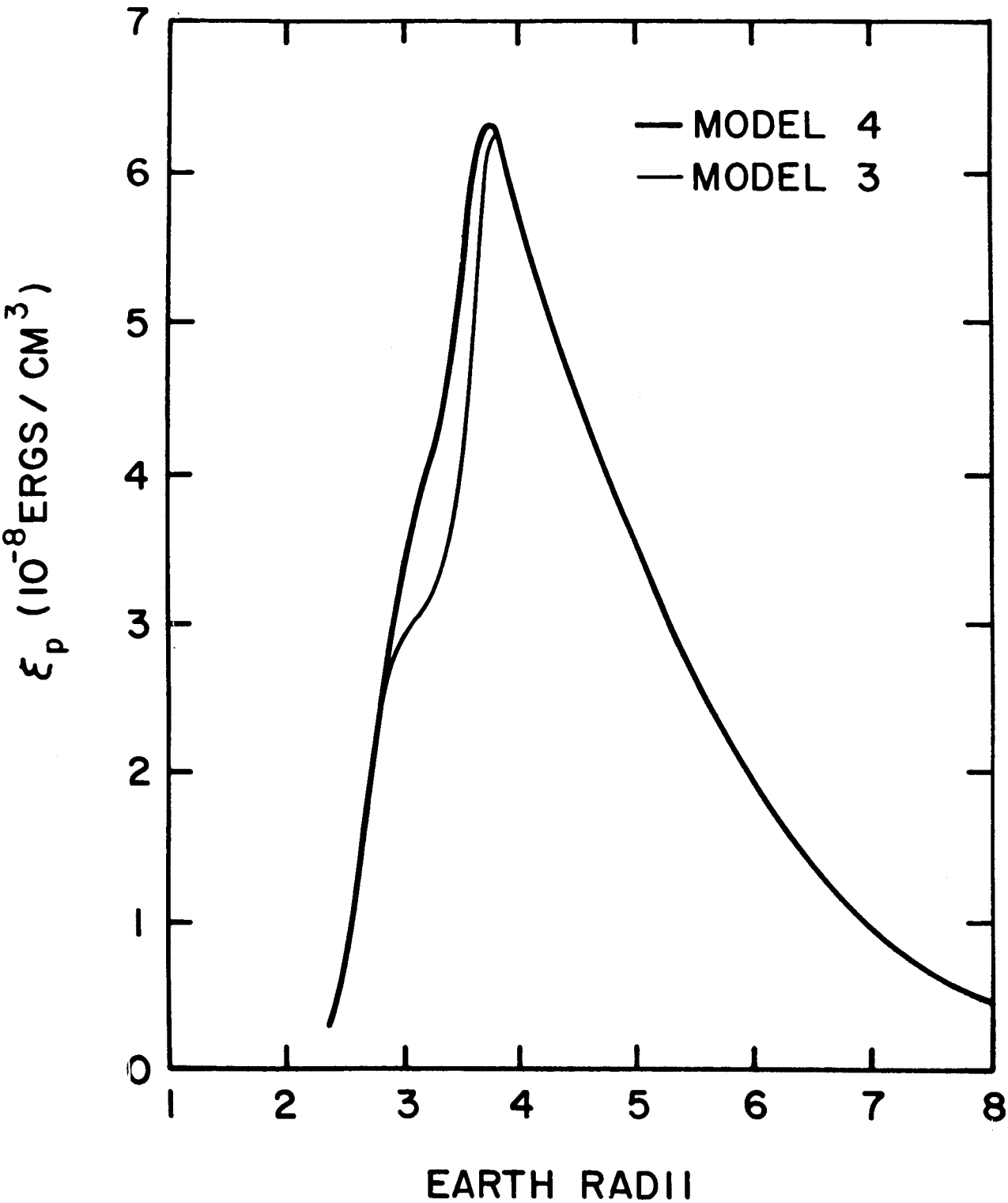
MODEL 4
MODEL 3
$\mathcal{E}_p$ (10^{-8}ERGS / CM^3)
EARTH RADII
0
1
2
3
4
5
6
7
8

Figure 13

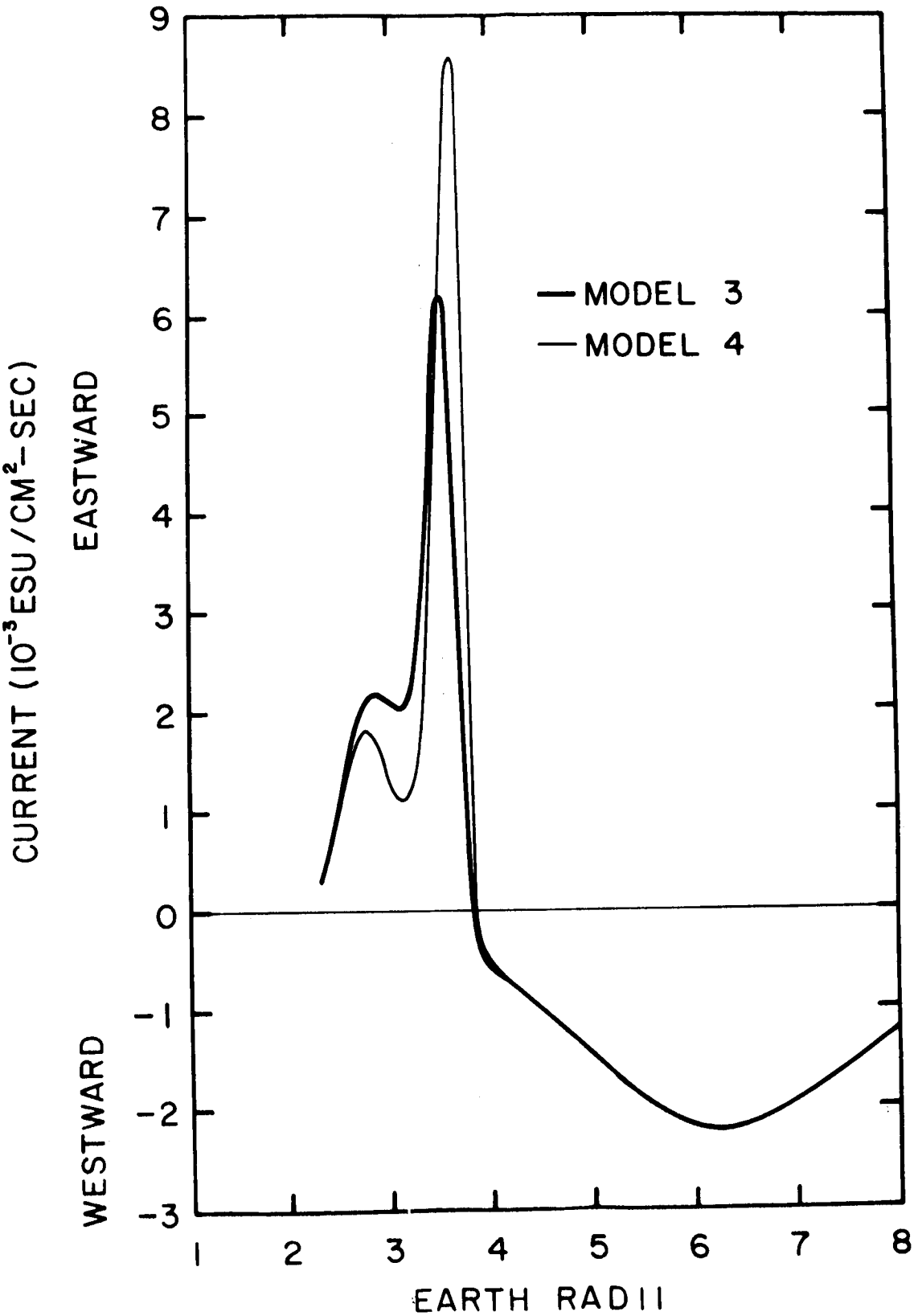
MODEL 3
MODEL 4
CURRENT (10^{-3}ESU/CM^2-SEC)
EASTWARD
WESTWARD
EARTH RADII
9
8
7
6
5
4
3
2
1
0
-1
-2
-3
1
2
3
4
5
6
7
8

Figure 14

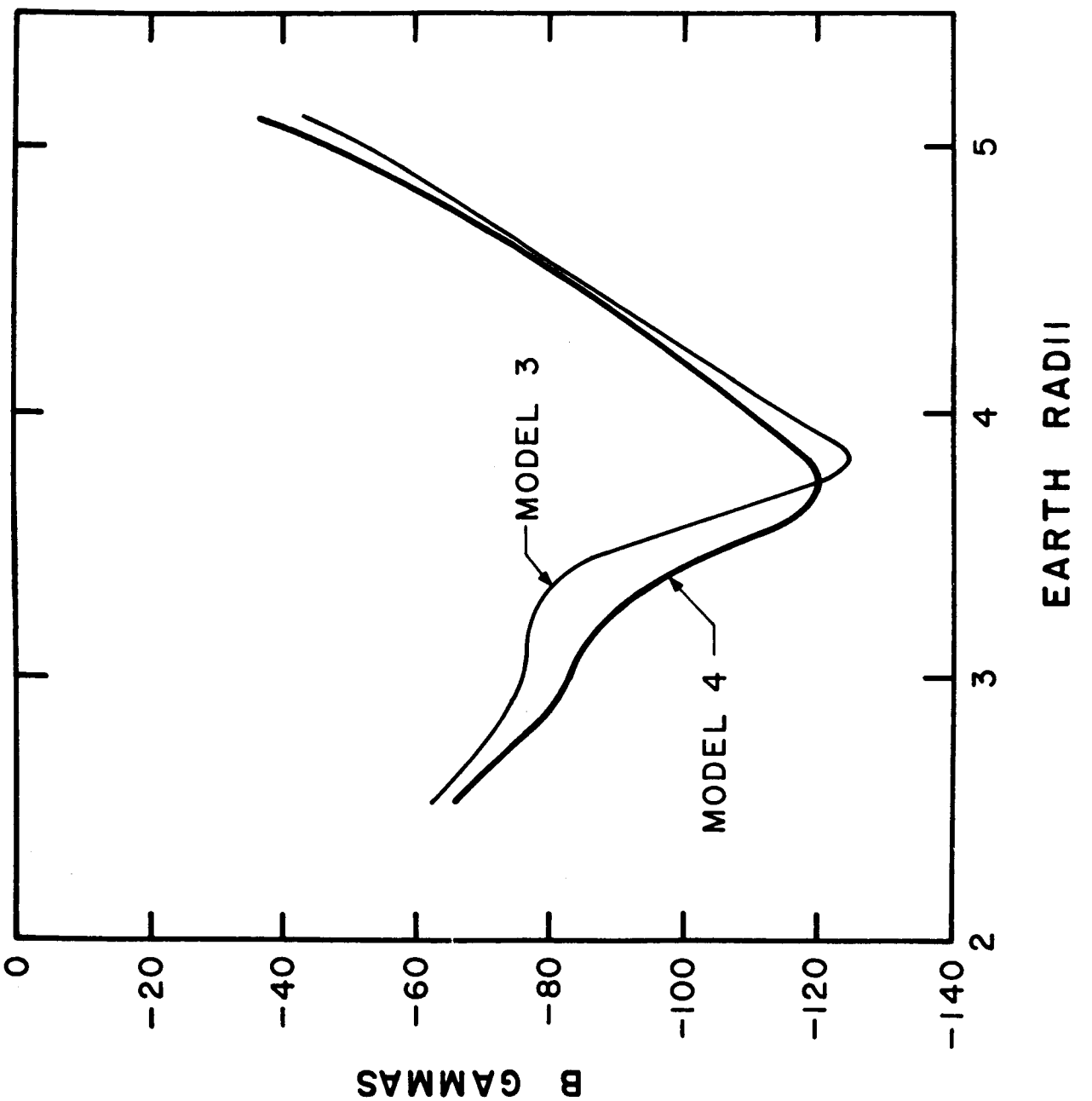
B GAMMAS
0
-20
-40
-60
-80
-100
-120
-140
2
3
4
5
EARTH RADII
MODEL 3
MODEL 4

Figure 15

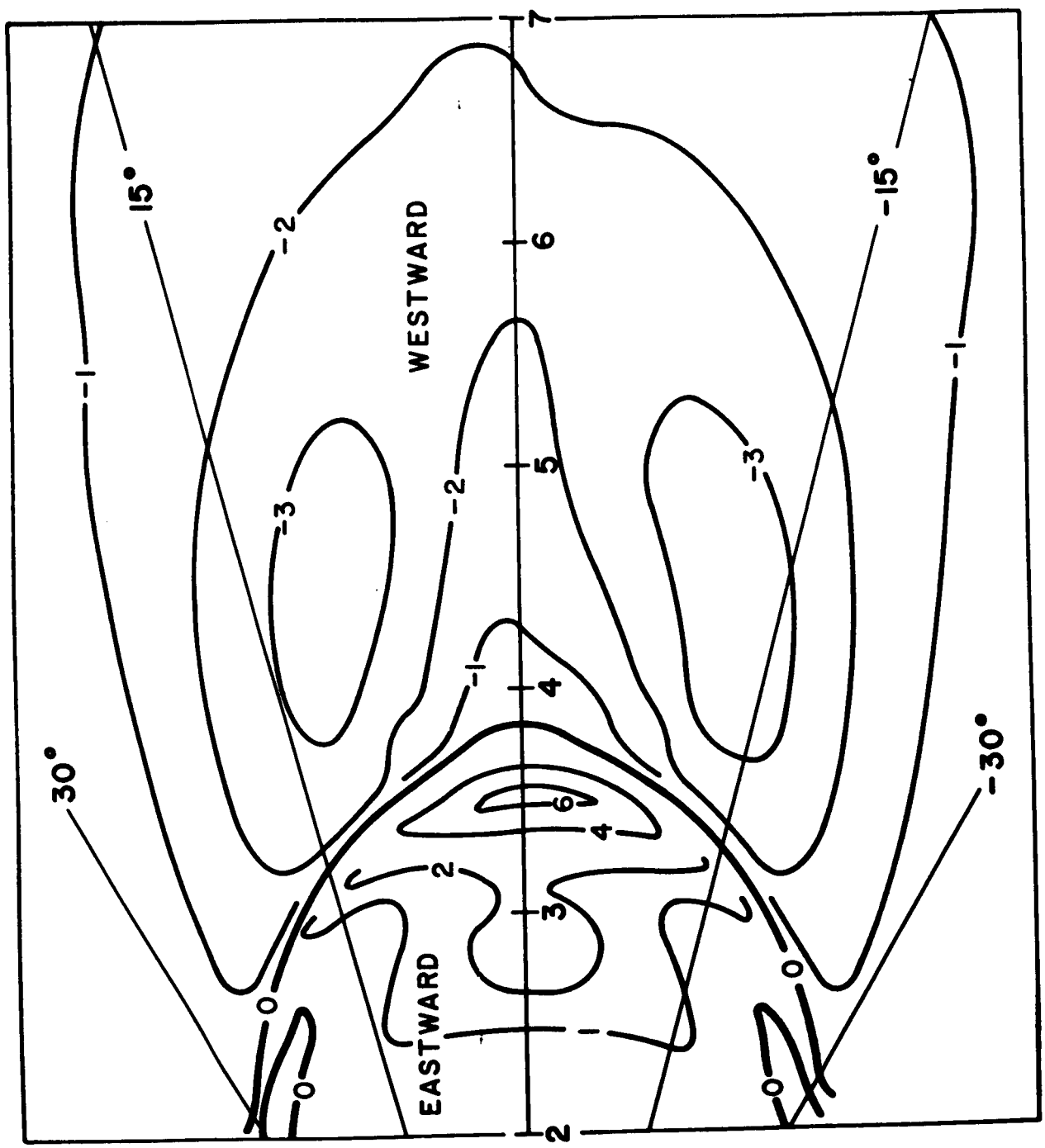

Figure 16